

Automatic Detection of Lumbar Anatomy in Ultrasound Images of Human Subjects

Denis Tran* and Robert N. Rohling, *Senior Member, IEEE*

Abstract—Ultrasound has been proposed for aiding epidural needle insertion, but challenges remain in differentiating spinal structures due to noise, artifacts, and inexperience by anesthesiologists in ultrasound interpretation. Moreover, the anesthesiologist needs to measure relevant distances while preserving sterile conditions; therefore, interaction with the ultrasound controls must be minimal. Automated measurement is needed. Beam-steered ultrasound images are captured and spatial compounding is used to improve image quality. Phase symmetry is used to enhance bone (lamina) and ligamentum flavum (LF) ridges. A lamina template is matched to this ridge map using Pearson's cross-correlation, and the most likely lamina positions are found. Then, the lamina is traversed using a LF template with the Pearson's cross-correlation, and the location of the LF is obtained. Tests are performed on 39 sets of compounded ultrasound images in the L2–3 and L3–4 levels of the spine in the paramedian plane. The proposed algorithm can detect the laminae in 38 of the 39 images, and the LF in 34 of the 39 images. In successful detections, the automatic detections versus manual segmentation has an rms error of 0.64 mm and average error 0.04 mm, versus independent sonographer-measured depth has a root-mean-squared error of 3.7 mm and average error 2.5 mm, and versus the actual needle insertion depth has a root-mean-squared of 5.1 mm and average error –2.8 mm. The computational time is 4.3 s on a typical personal computer. The accuracy, reliability, and speed suggest this method may be valuable for helping guide epidurals in conjunction with the traditional loss-of-resistance method.

Index Terms—Human subjects, lumbar epidurals, phase symmetry, ridge detection, spatial compounding, template matching.

I. INTRODUCTION

IN OBSTETRICS, a patient may require the use of epidural anesthesia to provide pain relief during labor and delivery. Administering lumbar epidural anesthesia is a challenging procedure. The correct needle insertion depth can range from 20 to 90 mm depending on the individual patient, and overshoot can result in spinal nerve injury [1]. This procedure is currently being done “blind” using only the sense of feel (loss-of-resistance) for

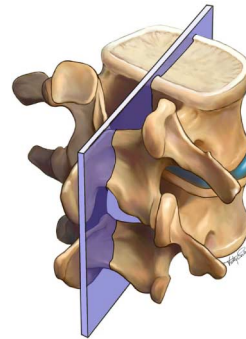


Fig. 1. Paramedian plane in lumbar vertebrae.

guidance. Ultrasound has been proposed to visualize structures in the lumbar anatomy [2]–[4], but structures are hard to depict due to speckle noise and artifacts. More recently, real-time ultrasound has been used to guide needle insertions in lumbar epidural anesthesia [5]–[7], however, the structures remained hard to depict and success of the procedure relies heavily on the experience of the anesthesiologist with ultrasound.

There has been earlier study [8] that shows the use of ultrasound to locate the puncture site, measure the expected puncture depth, and angle to optimize the puncture technique. The number of necessary puncture levels, visual analog scales and rate of side effects all decreased with the use of ultrasound, which shows the success of ultrasound usage in epidural anesthesia.

The paramedian plane is the optimal plane for ultrasound images of the lumbar anatomy [9]. Often, it takes time to scan and find this plane by positioning the transducer 2–3 mm lateral and angling 0°–10° midline [3]. Fig. 1 shows the paramedian plane of interest, which includes the laminae, the ligamentum flavum (LF), and the vertebral body (see Fig. 2).

An automatic method for detecting the laminae and LF would be useful for helping the anesthesiologist choose the proper paramedian plane and measure the skin-to-LF depth that represents the desired needle insertion depth from the skin surface. Moreover, needle insertions are performed in sterile environment, and the anesthesiologist needs to measure relevant distances while preserving sterile conditions; therefore, interaction with the ultrasound controls must be minimal. A fully automatic method is needed for measuring the desired needle insertion depth.

We will present such an automatic method based on the way the anesthesiologist identifies the features in the lumbar anatomy in the ultrasound image and recognizes the lamina and the LF. From the detected features, the skin-to-LF depth is calculated.

Manuscript received February 10, 2010; revised March 29, 2010; accepted April 13, 2010. Date of publication May 10, 2010; date of current version August 18, 2010. This work was supported by a Collaborative Health Research Project grant from the Natural Sciences and Engineering Research Council of Canada and the Canadian Institute of Health Research. Asterisk indicates corresponding author.

*D. Tran is with the University of British Columbia, Vancouver, BC V6T 1Z4, Canada (e-mail: denist@ece.ubc.ca).

R. N. Rohling is with the University of British Columbia, Vancouver, BC V6T 1Z4, Canada (e-mail: rohling@ece.ubc.ca).

Color versions of one or more of the figures in this paper are available online at <http://ieeexplore.ieee.org>.

Digital Object Identifier 10.1109/TBME.2010.2048709

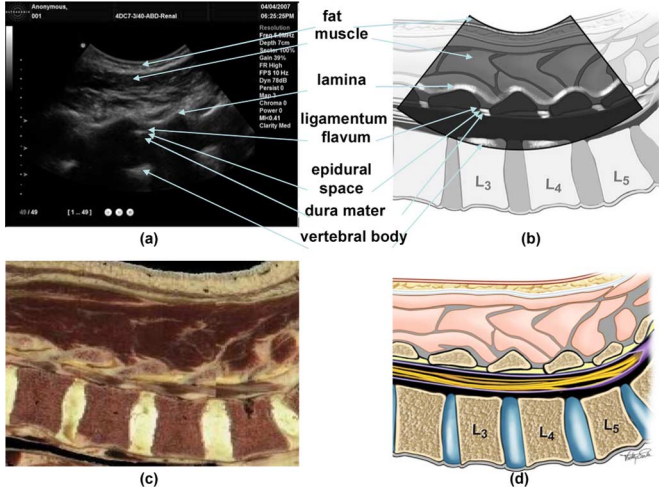


Fig. 2. (a) Ultrasound image of paramedian plane of the lumbar anatomy. (b) Idealized ultrasound image of the anatomy. (c) Slice through the Visible Human [10] at the location of the lumbar anatomy. (d) Pictorial view of the corresponding lumbar anatomy.

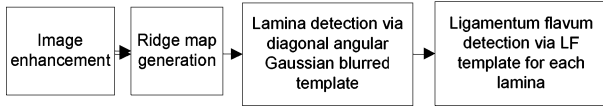


Fig. 3. Overview of LF detection algorithm.

II. METHODS

A. Overview of Algorithm

Fig. 3 shows an overview of the algorithm used to estimate the skin-to-LF depth. The first step is to acquire beam-steered images and use spatial compounding with warping and combine them using the adaptive median [11]. The purpose is to improve the uniformity of the lamina and LF. Phase symmetry [12] is then used to extract the lamina and LF from this enhanced image in a ridge map. A template-matching algorithm is then used to segment out the laminae from the ridge map. The LF is subsequently segmented from the image using another template around the lamina. The skin-to-LF depth is finally measured. Each step is now explained in detail.

B. Image Enhancement

Ultrasound speckle in the image often obscures the LF, which appears as a short bright feature on a scale slightly larger than speckle. Steering the ultrasound beam electronically is one method of discerning the LF echo because the speckle decorrelates with beam angle, while the LF remains stationary. At some beam angles, the LF appears more clearly than at other angles [11]. The other lumbar anatomy visibility also depends on the angle of incidence of the ultrasound beam; therefore, acquiring images at different angles should facilitate automatic feature detection. Spatial compounding [13] is a process by which several images of the same anatomy are taken at different beam-steered angles and combined (compounded) together. In this application, the images are first warped to realign the struc-

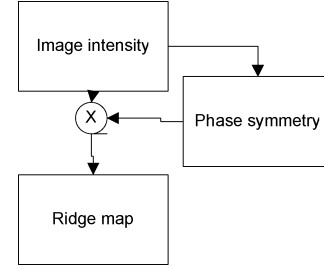


Fig. 4. Flowchart of the ridge map generation.

tures and then compounded using the adaptive median [11]. Adaptive median combination of warped beam-steered images has been shown to improve the SNR of ultrasound images of the lumbar anatomy while retaining the sharpness of the features.

Warping is done through block matching of beam-steered images to a reference image (zero beam angle), using the Pearson cross-correlation as the similarity measure

$$R_I(i, j) = \frac{\sum_{i,j} (I_{i,j}^{\text{beam}} - \mu_{I^{\text{beam}}}) (I_{i,j}^{\text{ref}} - \mu_{I^{\text{ref}}})}{\sqrt{\sum_{i,j} (I_{i,j}^{\text{beam}} - \mu_{I^{\text{beam}}})^2 \sum_{i,j} (I_{i,j}^{\text{ref}} - \mu_{I^{\text{ref}}})^2}} \quad (1)$$

where $R_I(i, j)$ is the correlation coefficient of the beam-steered image I^{beam} to the reference image I^{ref} , $I_{i,j}^{\text{beam}}$ is the pixel at location (i, j) of the block in the beam-steered image, $\mu_{I^{\text{beam}}}$ is the average of the block in the beam-steered image, $I_{i,j}^{\text{ref}}$ is the pixel at location (i, j) of the block in the reference image, and $\mu_{I^{\text{ref}}}$ is the average of the block in the reference image.

The block sizes and other parameters are identical to the values used earlier [11].

C. Feature Detection

For bone detection, Canny [14] and other gradient-based methods are too dependent on the choice of parameters and thresholds [12], [15]. There is a need for a technique independent of image intensity because the ultrasound intensity changes with the time-gain compensation curves and image-depth parameters selected by the operator.

Phase is suggested to often contain more information than magnitude [16]. Recently, phase techniques have gained popularity as they perform very well at detecting bones in ultrasound images [12]. As the lamina and LF have the appearance of a ridge, phase symmetry is used because it is a phase-based measure designed to detect ridges (see Fig. 4) [17]. Phase symmetry is defined as

$$PS(x) = \frac{\sum_n [|e_n(x)| - |o_n(x)|] - T}{\sum_n A_n(x) + \varepsilon} \quad (2)$$

where ε is a small constant to prevent division by 0, T is a threshold used to offset the phase symmetry by the expected noise value

$$T = \mu_R + k\sigma_R \quad (3)$$

where k is a user defined variable, μ_R and σ_R are the mean and standard deviation of the Rayleigh distribution of the noise energy response, respectively. We are interested in the distribution

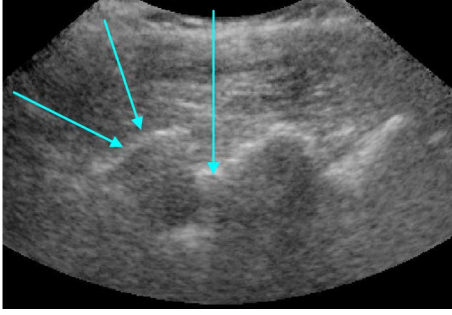


Fig. 5. Orientations of the Log-Gabor filter used for phase symmetry (90° , 120° , and 150°).

of magnitude $A_n(x)$ of the energy vector [15]

$$A_n(x) = \sqrt{e_n(x)^2 + o_n(x)^2} \quad (4)$$

where $e_n(x)$ is the even part of the signal and $o_n(x)$ is the odd part of the signal produced by the Log-Gabor filter

$$[e_n(x), o_n(x)] = [I(x) * M_n^e, I(x) * M_n^o]. \quad (5)$$

The Log-Gabor filter $G(\omega)$ is used to extract the even and odd parts to be used in the phase measures and is defined as

$$G(\omega) = \exp\left(\frac{-(\log(\omega/\omega_o))^2}{2(\log(k/\omega_o))^2}\right) \quad (6)$$

$$M_n^e = \text{Re}(F^{-1}(G(\omega)))$$

$$M_n^o = \text{Im}(F^{-1}(G(\omega))) \quad (7)$$

where k/ω_o is a ratio to be held constant for constant shape ratio filters, and ω_o is the filter's center frequency. $G(\omega)$ is the Log-Gabor filter and $F^{-1}(G(\omega))$ is the inverse Fourier transform of $G(\omega)$.

The filters were run on a test image of the lumbar anatomy, and it was observed that some filter orientations did not contain information on the ridges of interest (lamina and LF) as the features mostly appeared at specific orientation angles (near oblique to the ultrasound beam). Only three orientations (90° , 120° , and 150°) (shown in Fig. 5) are needed.

The 192 line prescan-converted images are acquired with a resolution of 0.3125 mm/pixel and a depth varying between 60 and 120 mm depending on the subject. By performing the autocorrelation in the axial direction of a small block containing only speckle, we obtain a speckle size of approximately 7–9 pixels. The minimum wavelength of 15 pixels was used to avoid response from speckle at different angles. We used three scales with a multiplier of 2.1 between the wavelengths of each scale. The Log-Gabor filter was designed with a sigma on frequency (frequency spread) of 0.65 and theta on sigma (angular spread) of 1.5. These parameters are determined experimentally to result in minimal overlap necessary to achieve even spectral coverage using a Log-Gabor filter bank. The value of k used for noise threshold is also determined experimentally and is set to 5 [15]. For bone detection in ultrasound, these parameters are similar to those used earlier in other applications [12]; therefore, the algorithm does not require parameter tuning to a specific subject.

In the ultrasound image (see Fig. 2), the lamina and LF can also be seen by their bright edges relative to the muscle, creating high-intensity ridges. The phase symmetry is multiplied with the amplitude of the image and is called the ridge map (see Fig. 4).

D. Lamina Extraction

The lamina and LF need to be extracted from the ridge map. The lamina is defined geometrically by a slightly curved line (see Fig. 2). Because of the variable curved nature of the lamina that depends on each patient and transducer placement, a template matching with a wide-angle capture range approach is used in this paper.

A diagonal line of angle matching the average of the lamina angles is blurred by a Gaussian filter, where the angle of the diagonal line has a Gaussian shape with standard deviation depending on the expected range of lamina angles. This is determined by manually measuring the angles of the ridge map from an earlier study [3]. The angles for the lamina are measured to be 32° (μ_{lam}) with standard deviation 11.2° (σ_{lam})

$$F(r, \theta_{\text{lam}}) = \frac{1}{\sqrt{2\pi}\sigma_{\text{lam}}} \exp\left(-\frac{(\theta_{\text{lam}} - \mu_{\text{lam}})^2}{2\sigma_{\text{lam}}^2}\right). \quad (8)$$

Additionally, the diagonal angular Gaussian blurred filter is blurred in the direction perpendicular to its length by a thickness blur in order to widen the capture range. $F(r, \theta_{\text{lam}})$ is the function defining the angular Gaussian blurred filter, μ_{lam} and σ_{lam} are the average and standard deviation of the angles of the laminae, respectively. θ_{lam} is the angle in the lamina template defined in polar coordinates equivalent to $\theta_{\text{lam}} = \tan^{-1}(y/x)$. r is the radius from the center, but is not used in the formula.

$S(x, y)$ is the function defining the thickness Gaussian blurring filter [18], μ_{thick} is the average thickness of the laminae in the ridge map

$$S(x, y) = \frac{1}{\sqrt{2\pi}\mu_{\text{thick}}} \exp\left(-\frac{(y)^2}{2\mu_{\text{thick}}^2}\right) \quad (9)$$

where $S(x, y)$ is rotated by a rotation matrix

$$\begin{bmatrix} x' \\ y' \end{bmatrix} = \begin{bmatrix} \cos(\mu_{\text{lam}} + 90^\circ) & -\sin(\mu_{\text{lam}} + 90^\circ) \\ \sin(\mu_{\text{lam}} + 90^\circ) & \cos(\mu_{\text{lam}} + 90^\circ) \end{bmatrix} \begin{bmatrix} x \\ y \end{bmatrix} \quad (10)$$

and therefore, it follows the direction perpendicular to the angular Gaussian blurring filter $F(r, \theta_{\text{lam}})$ and becomes $S(x', y')$. μ_{thick} is measured to be 2.1 pixels from extracting the ridge map of a wire phantom and measuring the thickness of the response from a point, assuming the response to be Gaussian shape, 2σ (or $2\mu_{\text{thick}}$ in this application) would be the point, where the response falls to 5%. This is the lamina template T^{lam}

$$T^{\text{lam}} = F(r, \theta_{\text{lam}}) * S(x', y'). \quad (11)$$

The lamina template size is 41×41 , which is sufficiently loose to capture a single lamina in adults.

This template is matched to the image using the Pearson correlation (1) [19] and a lamina similarity map is generated. The template is shown in Fig. 6(a). An image can contain more than one lamina [3]. From the knowledge of adult anatomy

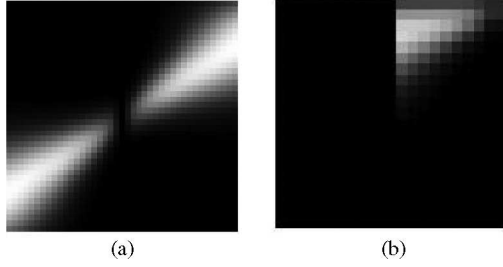


Fig. 6. (a) Template for the detection of the lamina (41×41 pixels) composed of a line with an angular Gaussian blur and a diagonal thickness blur. (b) Template for the detection of the LF (21×21 pixels) composed of a line from the corner to halfway through the template to detect an end of the line; the line is also blurred with an angular Gaussian blur and a diagonal thickness blur.

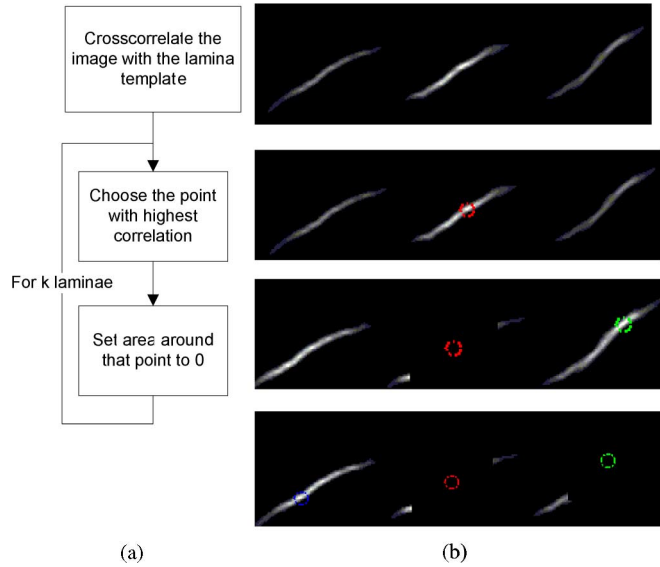


Fig. 7. (a) Flowchart of the search for the laminae. (b) Steps of the search for laminae from top row to bottom: choose the point of highest lamina correlation, set the area around that point to zero, and choose the next point of highest correlation. The circles denote the positions of three laminae.

and practical experience with ultrasound of the spine, the adult subjects in this study have at most three laminae in the ultrasound image with a skin-to-LF depth ranging from 30 to 80 mm [3], although up to five are allowed by the algorithm. The areas of highest correlation in the lamina similarity map are chosen as the potential locations of the laminae: the highest similarity point in the image is chosen as the location of the first lamina; then, as the distance between two laminae is approximately 30 mm [6], the search region for the second lamina is set to at least 20 mm away from the first lamina location. This is repeated for as many laminae that we want to find. The search for the lamina locations with an example is depicted in Fig. 7.

E. LF Detection

For manual detection, after finding the lamina, the sonographer mentally locates the LF by following the lamina down and searching for the LF around the tip of the lamina because the LF attaches two laminae together. The automated algorithm follows a similar approach. The LF template is similar to the template

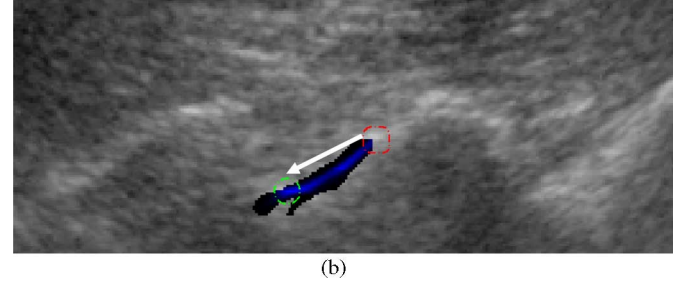
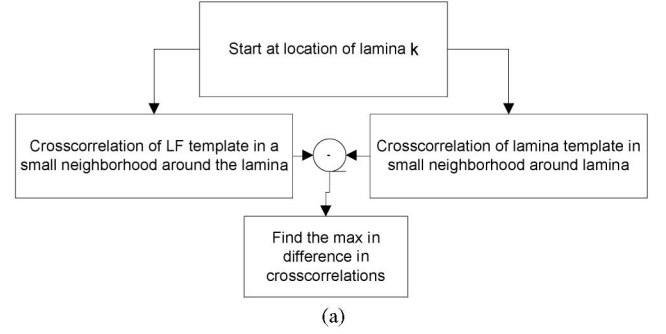


Fig. 8. (a) Flowchart for the search of the LF k . (b) Region below the position of the lamina is correlated with the lamina template and the LF template and the highest point of the difference between the two correlations is chosen as the position of the LF.

for the detection of the lamina in that it is a line with Gaussian cross section; however, the LF is often a line of different thickness and angle than the lamina. The angles for the LF of adults are measured to be 13.2° with a standard deviation 12.7° [3]. σ_{thick} is set to 2.1 pixels as well. Moreover, the template for the LF needs to locate the end of the ridge. A different template is used. The template is shown in Fig. 6(b). The cross-correlation R_{LF} of the LF template with the ridge map is only computed for pixels around the lamina. The LF detector looks for the point with the largest difference between R_{LF} and R_{lam} to emphasize the end of the ridge requirement defined as

$$\text{LF}_k(x, y) = \arg \max_{i, j} (R_{\text{LF}}(i, j) - R_{\text{lam}}(i, j)) \quad (12)$$

where $\text{LF}_k(x, y)$ is the location of the k th LF.

The search for the LF with an example is shown in Fig. 8. The template size is 21×21 for the LF template, which is sufficient for adults.

F. Performance Measures

The correctness of the LF detection was measured manually by visual inspection of the results. The LF was considered detected successfully, if the detection was on the body of the LF.

In order to assess the accuracy of the algorithm, the calculated distance from skin to LF was compared to three other measures: manual segmentation of the same ultrasound image, independent sonographer prepuncture examination measurement on a different image, and the actual needle-insertion depth measured by the anesthesiologist. The average error, rms error, and the Bland–Altman 95% limits of agreement were calculated on

correctly identified LF. Although the images can contain three LF, only the measurements for the most central LF were used because it is the one measured by the sonographer and to which the anesthesiologist inserted the needle.

Finally, the computational cost was measured. The algorithm was written in MATLAB (The Mathworks, Natick, MA) except for the spatial compounding, which was written in C++. The algorithm was tested on 262×500 images, searching for five potential LFs. The code was run on an Intel Core 2 Quad CPU at 2.83 GHz with 3.25-GB RAM.

G. Statistical Significance

The paired t -test was used to assess the statistical significance of the difference between the skin-to-LF depths measured by the algorithm, manually, by the sonographer and the needle-insertion depth. On those measurements, the omnibus K^2 test was performed [20] to verify normality of the data.

H. Clinical Trial

Ethical approval was obtained from the Clinical Review Ethics Board of the British Columbia Women's Hospital and Health Center (C05-0409) to perform ultrasound scans on 20 parturients in labor or scheduled for cesarean delivery. Informed written consent was obtained for all subjects. Two sets of images were recorded on L2-3 and L3-4 on each subject except for one case in which only L2-3 was recorded ($n = 20 \times 2 - 1 = 39$) due to time constraints. The sonographer was unable to measure the skin-to-LF depth on one of the 39 cases; therefore, 38 measurements are available.

The exclusion criteria were the usual contraindications to neuraxial anesthesia and the inability to speak English. Four subjects (1-4) went through labor and 16 subjects (5-20) went through Cesarean delivery, for which a combined spinal-epidural anesthesia was administered. Needle insertion was guided by the loss-of-resistance technique, using saline and continuous pressure on a glass syringe plunger.

The same anesthesiologist (Kamani) performed all epidural needle insertions. Scanning and data capture were performed by an experienced registered diagnostic medical sonographer (Lessoway) using an Ultrasonix RP500 and a 1-5-MHz broadband curvilinear transducer (Ultrasonix Medical Corp., Richmond, BC, Canada). The sonographer performed the measurements directly on the ultrasound image and performed the image capture for the offline processing at a later time.

III. RESULTS

Twenty parturient subjects were recruited and the subject biometrics are shown in Table I. Tests were run on 39 sets of images of varying image quality. The proposed method successfully detected the LF in 34 cases out of 39 (87%). Fig. 9 shows the intermediate images throughout the automatic detection of the LF. Among the five failed detections, one case misdetected the vertebral body as the LF because the lamina was not properly detected above the LF [see Fig. 10(a)], three had a disconnected lamina-LF complex and very poor image quality

TABLE I
PATIENT DETAILED INFORMATION

patient	age	weight	height	BMI	success	
1	35	62	168	22	Y	N
2	32	62	160	24.2	Y	N
3	33	80	157	32.5	Y	Y
4	40	66	157	26.8	Y	Y
5	37	70	164	26	Y	N
6	36	73	179	22.8	Y	Y
7	40	56.5	155	23.5	Y	Y
8	35	100	162	38.1	Y	Y
9	36	55	160	21.5	Y	Y
10	36	84	166	30.5	Y	Y
11	35	82.5	169	28.9	Y	Y
12	33	86	155	35.8	Y	Y
13	30	74	169	25.9	Y	Y
14	33	114	149	51.3	N	N
15	38	91	170	31.5	Y	Y
16	32	62	155	25.8	Y	Y
17	44	64	166	23.2	Y	Y
18	34	61	157	24.7	Y	Y
19	23	71	163	26.7	Y	Y
20	38	86	150	38.2	Y	Y

Success column shows success of the LF detection on each of the two datasets of one patient.

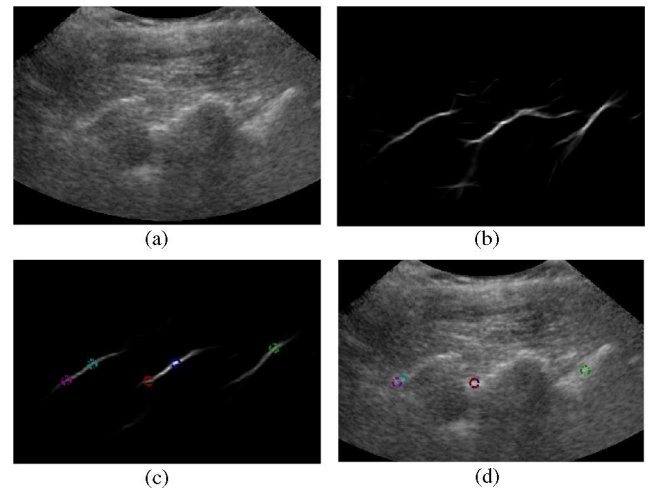


Fig. 9. (a) Spatial compounded image of a typical subject. (b) Ridge map. (c) Lamina similarity map and five strongest points of correlation. (d) Five most likely position of the LF. Note that there are cases where one lamina contains two of the five positions; in those cases, the same position for the LF is chosen twice.

[see Fig. 10(b)-(d)], and one image had no discernable LF [see Fig. 10(e)]. The low-quality images [see Fig. 10(d) and (e)] were of an obese subject with a significant layer of fat (16 mm).

The accuracy on the 34 successful detections of the LF is shown in Table II. The rms error of manual versus automatic detection of the LF is 0.64 mm (equivalent to 2 pixels), the average error is 0.04 mm, and 95% limits of agreement of -1.3 – 1.4 mm. The rms error of the automatic detection of the LF versus sonographer measurement of the distance on a different image during the prepuncture examination is 3.7 mm, equivalent to 10 pixels, the average error is 2.5 mm (an overestimate from the automatic detection algorithm), and 95% limits of agreement of -3.1 mm to 8.1 mm. The rms error between the automatic detection of the LF versus the needle-insertion depth as measured by the

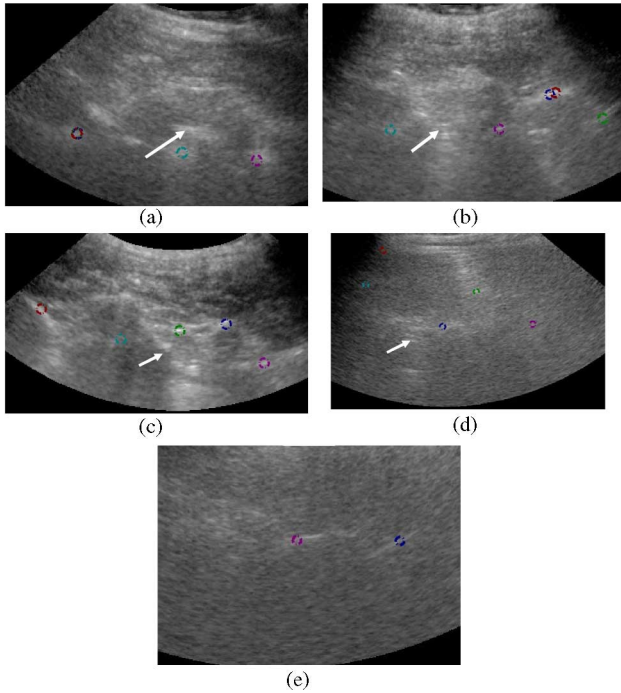


Fig. 10. Five cases of failed LF detection. (a) In this image, the region directly underneath the LF was detected as a lamina and the search for the LF found the vertebral body as the LF (image set 2). (b) Structures were hard to discern; no lamina was detected on top of what was manually chosen as the lamina (image set 3). (c) Structures were hard to discern, but a few laminae were still found (image set 9). (d) Lamina is not connected to the LF; therefore, the search found the position of the lamina (image set 27). (e) Case of low image contrast, no discernible LF. The lamina was found, but could not lead to the LF (image set 28). The white arrow denotes the actual location of the LF as determined by manual segmentation.

TABLE II

ACCURACY OF THE AUTOMATIC DETECTION OF LF COMPARED TO MANUAL SEGMENTATION, SONOGRAPHER MEASUREMENTS, AND ANESTHESIOLOGIST NEEDLE-INSERTION DEPTH

Automatic detection versus	RMS error (mm)	Average error (mm)	Bland-Altman 95% limits of agreement (mm)
Manual detection	0.64	0.04	-1.3 to 1.4
Sonographer prepuncture examination	3.7	2.5	-3.1 to 8.1
Needle insertion depth	5.1	-2.8	-12.3 to 6.7

anesthesiologist is 5.1 mm, equivalent to 16 pixels, the average error is -2.8 mm (an underestimate from the automatic detection algorithm), and 95% limits of agreement of -12.3 mm to 6.7 mm. The Bland-Altman plots are shown on Fig. 11.

Computational costs for the main functions are measured and shown on Table III. The cost breakdown for compounding can be found in [11]. The three main operations of the detection algorithm are the phase symmetry (0.454 s), the lamina template cross-correlation (3.019 s), and the LF template cross-correlation (0.392 s).

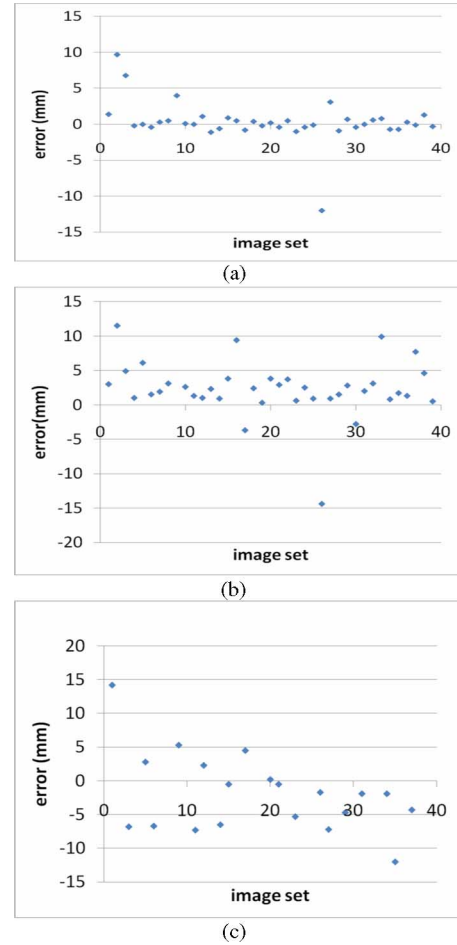


Fig. 11. Bland-Altman plots of automatic detection versus (a) manual segmentation ($n = 39$, 2 interspaces per subject except one case), (b) sonographer measurements ($n = 38$, the sonographer was unable to measure the LF depth in one case), and (c) needle insertion depth ($n = 20$, only defined for one interspace per subject as only one insertion was performed).

TABLE III

COMPUTATIONAL COST OF AUTOMATIC DETECTION OF LF USING MATLAB ON AN INTEL CORE 2 QUAD CPU AT 2.83 GHz WITH 3.25-GB RAM ON A 262×500 PIXELS IMAGE, SEARCHING FOR 5 LF

Function	Computational cost (s)
Template matching of the lamina	3.019
Template matching of the LF	0.392
Phase symmetry	0.454
Median-based spatial compounding	0.412

IV. DISCUSSION

In 31 cases, the algorithm detects other LFs in addition to the central LF, as there can be more than one foramina observed on each image. The algorithm was set to detect the five most likely positions of the LFs (see Fig. 9). If phase symmetry provides a ridge map corresponding to the lamina and LF, the lamina will be detected and the ridge will be followed until it reaches the LF, or will remain at the edge of the lamina, if the LF is missing or disconnected [see Fig. 10(d) and (e)].

Looking at the cases, where the automatic detection algorithm failed (see Table I), only one of the four subjects with failures

was obese (defined as Body Mass Index (BMI) > 30 [21]). Six other obese subjects were successful in automatic detection; therefore, there does not appear to be a relationship between obesity and success of the detection algorithm. On the other hand, the subject that produced failures on both automatic detection attempts had a BMI of 51.3, which is much larger than all other subjects, and the image quality was relatively poor. It is possible that patients with very high BMI still present a challenge to the algorithm because very large imaging depths produce images with poorer image quality. To investigate this issue further, the thickness of the fat layer above the epidural space in the ultrasound image was manually measured for each subject because obesity may not correlate with fat thickness on the back. Indeed, the subcutaneous fat thickness only had a correlation coefficient of $R^2 = 0.71$ with obesity. It is observed from the data that out of seven subjects with a fat thickness greater than 5 mm, only one case had a failed LF detection, whereas for fat thickness less than 5 mm, 3 out of 13 cases had a failed LF detection. In summary, it is more appropriate to state that the success of the LF detection depends mainly on the ultrasound image quality, but is not directly related to obesity or fat thickness. This means that the automatic detection algorithm may provide valuable assistance on those patients, where epidural needle-insertion targeting is difficult. Since there is still a tradeoff between the benefit of ultrasound guidance, versus the additional equipment, training, and time needed to perform the ultrasound scan, it is expected initially that ultrasound will be used mainly on patients after a failed insertion with the traditional loss-of-resistance technique. As more anesthesiologists gain experience with ultrasound, ultrasound may be used more frequently as a prepuncture-imaging technique to identify and assist “difficult” patients. Given the simultaneous current trends of increasing dissemination of ultrasound in anesthesiology, and miniaturization/cost-reduction of ultrasound scanners, ultrasound may eventually be used on a wide range of patients, but likely still coupled with the loss-of-resistance technique.

All measures are normally distributed as shown by the omnibus K^2 test. The bias was only 0.04 mm between the automatic detection and the manual detection of the LF and is not statistically significant ($p > 0.05$). There is a significant error of 2.5 mm overestimate ($p < 0.001$) of the skin-to-LF depth when comparing the sonographer and the automatic detection measurements. Most of this error likely arises because the sonographer always measured the depth from the skin to the leading edge of the LF, as opposed to the algorithm, which was designed to locate the central part of the LF. The average thickness of the LF echo measured on the ultrasound images is 2.6 mm, and the actual thickness of the LF is 5.0–6.0 mm [1]. There is also a significant error ($p < 0.03$) of -2.8 mm when comparing the anesthesiologist needle-insertion depth and the automatic detection is an underestimate of the skin-to-LF depth, and this also likely reflects the difference in measurement method. This is expected because the anesthesiologist inserts the needle until the tip passes the LF and goes into the epidural space, experiencing the loss of resistance thereafter to confirm the entry into the epidural space [1]. This means the distance measured by

the anesthesiologist is the skin to epidural space depth, whereas the automatic detection is measuring the distance from the skin to the middle of the LF and the sonographer is measuring the distance from skin to top of the LF.

There is also an rms error between the automatic detection and the sonographer (3.7 mm). It has been shown that the repeatability of a measurement by a sonographer is about 4.75%–7% [22]. The average skin-to-LF depth in this study was 46.2 mm; therefore, an intraobserver repeatability error around 2.2–3.2 mm is reasonable. The rms error between the automatic detection and anesthesiologist-measured needle-insertion depth is 5.1 mm. In addition to the bias discussed earlier, the ultrasound is in the paramedian plane and the needle insertion is performed in the midline. These sources of error are explored in more detail in [3].

The compression from the ultrasound transducer can cause a small but significant difference in the measurement of the skin-to-LF depth. Tran *et al.* [6] measured that the skin-to-LF depth changed by 2.8 mm on average (6.4%), on an average skin-to-LF depth of 43.8 mm.

The majority of computation time is spent on the Pearson cross-correlation to match the lamina template to the ridge map (3.0 s), thus obtaining the lamina similarity map. Replacing the MATLAB implementation with C++ will reduce this to about 70 ms. The correlation can also be performed on a coarse-resolution ridge map, as the position of the lamina is not required to be precise. Overall computation cost can also be reduced by defining a region of interest. Computational speed should be judged sufficient, if the algorithm can run in less than 1 s on a general-purpose CPU with additional hardware or acceleration techniques. The automated algorithm can achieve this goal on the CPU of a machine comparable to the ultrasound machine used in this study. Other ultrasound machines have similar performance; therefore, the algorithm can be implemented on a wide range of ultrasound machines.

The typical weakness of many automated image interpretation algorithms is the need to tune the parameters for optimal performance on each image used. The parameters of the algorithm in this paper are set to values determined by the range of variation in geometry of adult lumbar anatomy. Ridge detection using phase symmetry uses volume similar to other bone-detection implementations. All parameters remained fixed for all subjects in this study. Failures are attributed to image and not to suboptimal parameter values.

Although the images were acquired by an experienced sonographer, the scanning parameters remained unchanged throughout the 20 subjects, with the exception of the depth and focus. It is expected that anesthesiologists can achieve comparable image quality to sonographers. In an earlier study with a similar scanning protocol, the sonographer was replaced with an anesthesiologist for real-time ultrasound guidance of epidural needle insertion [6]. The key is to learn the correct location where to place the probe to see the anatomy clearly, which is learned quickly by searching for the familiar wave-like pattern of the lamina, as explained in [6]. Moreover, it is suggested that anesthesiology residents, with little or no ultrasound experience, can rapidly learn and improve their speed and accuracy in performing a simulated interventional ultrasound procedure [23].

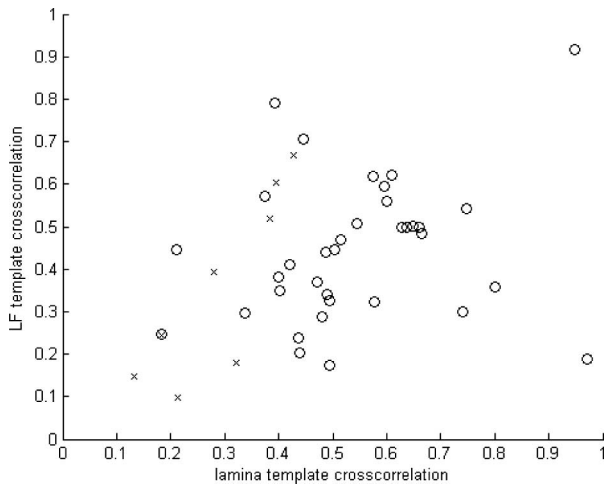


Fig. 12. Distribution of the LF detections in the cross-correlation with lamina and LF templates space. The circles are the successful detections and the crosses are the failed detections.

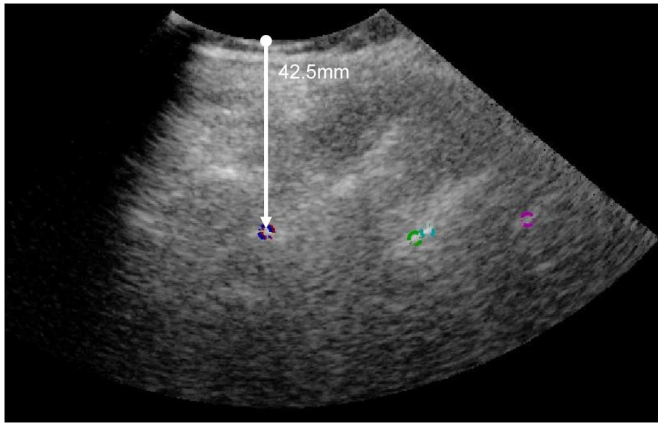


Fig. 13. Ultrasound image of the lumbar anatomy with the LF detected, showing the skin-to-LF depth and the automatic measurement as an overlay.

The user is expected to have an understanding of how to interpret the structures seen in the ultrasound image so that the results of the automatic detection algorithm can be assessed for possible failures. Since the automatic skin-to-LF depth measurement is shown as a graphic overlap on the ultrasound image, an incorrect identification of the LF should be obvious, if the overlay does not lie near the expected location of the LF relative to the lamina. As an additional measure, it may be possible to look at the level of cross-correlation with the lamina template and the LF template. Fig. 12 shows a distribution of the LF detections in the cross-correlation with the lamina and LF templates space. For these patients, a cross-correlation value of the lamina template greater than 0.5 was always associated with success of the algorithm. The display of the cross-correlation coefficient should, therefore, be investigated in future research.

A depiction of the ultrasound image with the LF detection and the measurement of the skin-to-LF depth are overlaid on the image, as shown in Fig. 13. This automatic LF detection can be used in the following proposed clinical protocol.

- 1) Place the ultrasound transducer in the paramedian plane over the target intervertebral level using the method described in [3] to identify the levels.
- 2) Show the ultrasound with overlay locating the LF.
- 3) Adjust transducer placement until the clearest view of the LF is obtained during prepuncture scanning; the anesthesiologist confirms that the LF is correctly identified by the algorithm and memorizes the provided skin-to-LF depth measurement for subsequent manual needle insertion without further use of ultrasound.

If ultrasound is used for real-time needle guidance, the anesthesiologist confirms that the LF is correctly identified by the algorithm and aligns the needle trajectory as shown in [6] with the LF.

The needle is inserted with precaution such that the actual needle insertion depth (using the markings on the needle) only comes close to the skin-to-LF depth measured on the image, and the traditional loss-of-resistance technique is used for the final approach. The needle tip is then placed between the LF and dura mater as confirmed by the loss-of-resistance technique.

V. CONCLUSION AND FUTURE WORK

An automatic algorithm can detect the lamina and LF and measure the skin-to-LF depth with a success rate of approximately 87% in adult subjects. The algorithm is meant to assist the anesthesiologist in quickly finding the epidural space and measure the skin-to-LF depth because of time limitations in the operating room and the need to remain sterile. Therefore, limited interaction with the ultrasound machine is required. It should be emphasized that this algorithm is meant to be an aid and not a replacement for image interpretation by the anesthesiologist. The presence of small errors and occasional failures to detect the LF mean the anesthesiologist should view the actual ultrasound image with the automated measurement shown as an additional guide. The algorithm uses image-processing techniques that can be implemented to run sufficiently fast on the general-computing hardware of typical ultrasound machines. Failures occurred mainly in images with poor image quality; therefore, continued improvement in image quality should also improve performance of the algorithm.

Current interest in ultrasound for epidural needle insertion is toward real-time needle insertion [6] in which in-plane needle insertion is performed with a needle guide and an associated predefined trajectory line. Future algorithms will look for the LF along a region of interest defined around this trajectory line used for real-time needle insertion, in which case there will not be any ambiguity about which is the LF of interest, as well as decreased computational cost.

ACKNOWLEDGMENT

The authors would like to thank V. Lessoway, the sonographer, and A. Kamani, the anesthesiologist, for acquiring the data. The authors would also like to thank V. Earles of the Media Graphics Group, University of British Columbia for drawing artistic renderings.

REFERENCES

- [1] D. H. Chestnut, *Obstetric Anesthesia: Principles and Practice*, 2nd ed. St. Louis, MO: Mosby Inc., 2004.
- [2] T. Grau, R. W. Leipold, R. Conradi, E. Martin, and J. Motsch, "Ultrasound facilitates localization of the epidural space during combined spinal and epidural anesthesia," *Reg. Anesth. Pain Med.*, vol. 26, pp. 64–67, Jan. 2004.
- [3] D. Tran, A. A. Kamani, V. A. Lessoway, C. E. Peterson, K. W. Hor, and R. N. Rohling, "Preinsertion paramedian ultrasound for epidural anesthesia," *Anesth. Analg.*, vol. 109, pp. 661–667, Aug. 2009.
- [4] C. Arzola, S. Davies, A. Rofaef, and J. C. A. Carvalho, "Ultrasound using the transverse approach to the lumbar spine provides reliable landmarks for labor epidurals," *Anesth. Analg.*, vol. 104, pp. 1188–1192, May 2007.
- [5] T. Grau, R. W. Leipold, S. Fatehi, E. Martin, and J. Motsch, "Real-time observation of combined spinal-epidural anaesthesia," *Eur. J. Anaesth.*, vol. 21, pp. 25–31, Jan. 2004.
- [6] D. Tran, A. A. Kamani, E. Al-Attas, S. Massey, V. A. Lessoway, and R. N. Rohling, "Single-operator real-time ultrasound guidance to aim and insert a lumbar epidural needle," *Can. J. Anesth.*, vol. 57, pp. 313–321, Apr. 2010.
- [7] M. K. Karmakar, X. Li, A. M. H. Ho, W. H. Kwok, and P. T. Chiu, "Real-time ultrasound-guided paramedian epidural access: Evaluation of a novel in-plane technique," *Br. J. Anaesth.*, vol. 102, pp. 845–854, Jun. 2009.
- [8] T. Grau, R. W. Leipold, R. Conradi, E. Martin, and J. Motsch, "Efficacy of ultrasound imaging in obstetric epidural anesthesia," *J. Clin. Anesth.*, vol. 14, pp. 169–175, May 2002.
- [9] T. Grau, R. W. Leipold, J. Horter, R. Conradi, E. O. Martin, and J. Motsch, "Paramedian access to the epidural space: The optimum window for ultrasound imaging," *J. Clin. Anesth.*, vol. 13, pp. 213–217, May 2001.
- [10] M. J. Ackerman, "The visible human project," *Proc. IEEE*, vol. 86, no. 3, pp. 504–511, Mar. 1998.
- [11] D. Tran, K. W. Hor, V. A. Lessoway, A. A. Kamani, and R. N. Rohling, "Adaptive ultrasound imaging of the lumbar spine for guidance of epidural anesthesia," *Comput. Med. Imag. Graph.*, vol. 33, pp. 593–601, Dec. 2009.
- [12] I. Hacıhaliloglu, R. Abugharbieh, A. J. Hodgson, and R. N. Rohling, "Bone surface localization in ultrasound using image phase-based features," *Ultrasound Med. Biol.*, vol. 35, pp. 1475–1487, Sep. 2009.
- [13] S. K. Jespersen, J. E. Wilhjelm, and H. Sillesen, "Multi-angle compound imaging," *Ultrason. Imag.*, vol. 20, pp. 81–102, 1998.
- [14] J. Canny, "A computational approach to edge detection," *IEEE Trans. Pattern Anal. Mach. Intell.*, vol. PAMI-8, no. 6, pp. 679–714, Nov. 1986.
- [15] P. D. Kovesi, "Image features from phase congruency," *Videre, J. Comput. Vis. Res.*, vol. 1, pp. 1–26, 1999.
- [16] A. V. Oppenheim and J. S. Lim, "The importance of phase in signals," *Proc. IEEE*, vol. 69, no. 5, pp. 529–541, May 1981.
- [17] P. Kovesi, "Symmetry and asymmetry from local phase," in *Proc. 10th Aust. Joint Conf. Artif. Intell.*, Dec. 2–4, 1997, pp. 185–190, Poster Papers.
- [18] L. Fan, P. Santago, W. Riley, and D. M. Herrington, "An adaptive template matching method and its application to boundary detection of brachial artery ultrasound scans," *Ultrasound Med. Biol.*, vol. 27, pp. 399–408, Mar. 2001.
- [19] P. Filev, L. Hadjiiski, B. Sahiner, H. P. Chan, and M. A. Helvie, "Comparison of similarity measures for the task of template matching of masses on serial mammograms," *Med. Phys.*, vol. 32, pp. 515–529, Feb. 2005.
- [20] R. B. D'Agostino, "An omnibus test of normality for moderate and large size samples," *Biometrika*, vol. 58, pp. 341–348, Aug. 1971.
- [21] World Health Organization, *Obesity: Preventing and managing the global epidemic: Report of a WHO Consultation on Obesity*. World Health Organization, Geneva, 1997.
- [22] P. V. Balint and R. D. Sturrock, "Intraobserver repeatability and inter-observer reproducibility in musculoskeletal ultrasound imaging measurements," *Clin. Exp. Rheumatol.*, vol. 19, pp. 89–92, Jan. 2001.
- [23] B. D. Sites, J. D. Gallagher, J. Cravero, J. Lundberg, and G. Blike, "The learning curve associated with a simulated ultrasound-guided interventional task by inexperienced anesthesia residents," *Reg. Anesth. Pain Med.*, vol. 29, pp. 544–548, Nov. 2004.



Denis Tran was born in Montreal, QC, Canada, in 1981. He received the B.Eng. degree in computer engineering and the M.Eng. degree in electrical engineering from McGill University, Montreal, in 2003 and 2005, respectively. He is currently working toward the Ph.D. degree at the University of British Columbia, Vancouver, BC, Canada.

His research interests include ultrasonography for epidural anesthesiology.



Robert N. Rohling (M'00–SM'10) received the B.A.Sc. degree in engineering physics from the University of British Columbia (UBC), Vancouver, BC, Canada, the M.Eng. degree in biomedical engineering from McGill University, Montreal, QC, Canada, and the Ph.D. degree in information engineering from the University of Cambridge, Cambridge, MA.

He was the Project Manager of 3-D medical imaging at ALI Technologies, Vancouver, BC, Canada during 1999 and 2000. He is currently an Associate Professor at UBC. He is the Coordinator of the Biomedical Engineering Option and Co-Coordinator of the Mechatronics program at UBC. He is also a Member of the Digital Imaging and Communications in Medicine (DICOM) on multidimensional interchange. His research interests include adaptive ultrasound, 3-D ultrasound, elastography, and image-guided surgery.